A macro-element model for multidirectional cyclic lateral loading of monopiles in clay

Ana M. Page[a,b], Gustav Grimstad[a], Gudmund R. Eiksund[a], Hans Petter Jostad[b]

[a] *Norwegian University of Science and Technology (NTNU), Trondheim, Norway*
[b] *Norwegian Geotechnical Institute (NGI), Oslo, Norway*

Abstract

This paper investigates numerically the impact of multidirectional cyclic loads on the response of a monopile in clay supporting an offshore wind turbine (OWT). The results indicate that multidirectional loading modifies the foundation stiffness and hysteretic damping, which affects the OWT eigenfrequencies and damping. Based on these results, a macro-element model to represent the monopile response in the time-domain integrated load simulations employed in OWT design is proposed and verified against finite element analyses (FEA). The verification indicates the macro-element can simulate the monopile response with almost the same accuracy as FEA, but with a considerable reduction in computational effort.

Keywords: Offshore Wind Turbine, Load Calculation Methods, Soil-Structure Interaction, Multidirectional loading, Monopile, Macro-element model

1. Introduction

The structural design of monopile-based Offshore Wind Turbines (OWTs) relies on integrated analyses tools that simulate the dynamic response of the entire OWT (including foundation, support structure and rotor nacelle assembly) in time-domain under combined aerodynamic and hydrodynamic cyclic loads [1]. Due to its impact on the global dynamics, the numerical modelling of the foundation is an essential part of the integrated model of the OWT [2]. Specifically, the foundation stiffness and foundation damping can affect the natural frequency and damping of the OWT system, and consequently the fatigue damage and the designed structural fatigue lifetime [3].

Considerable effort has been made to develop foundation models for integrated analyses that can provide accurate stiffness and damping for the cyclic loads acting on OWTs. Monopile-based OWTs are subjected to large cyclic horizontal loads, which results in large cyclic overturning moments at seabed. In comparison, the cyclic vertical load is relatively small [4]. Monopiles resist these loads by mobilising the lateral resistance in the soil. Several models have been proposed to represent the lateral foundation response in integrated analyses of OWTs [5, 6, 7, 8, 9]. Some of these models focus on providing accurate foundation stiffness [5, 6], while others focus on providing foundation damping [7, 8]. A foundation model that can provide both accurate foundation stiffness and foundation damping is the macro-element model presented in Page et al. [9].

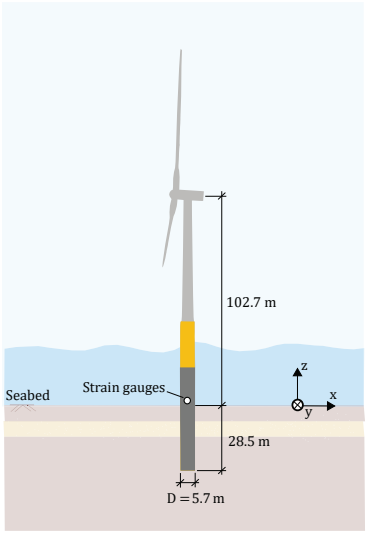

(a) Position of the strain gauges

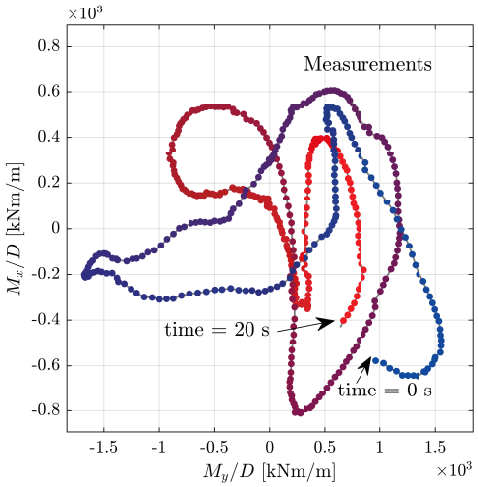

(b) Moments derived from strain gauge measurements

Figure 1: Illustration of the position of strain gauges at an OWT installed in the North Sea, and derived measured moments at seabed (M_x and M_y normalised by the pile diameter D).

However, most of these models assume that the loads are mainly applied in-plane and that the response in perpendicular planes is uncoupled. This is a clear simplification of the actual loading conditions, which are multidirectional in nature: waves do not reach the OWT in a unique direction, and there is misalignment between wind and waves. The multidirectional nature of these loads is illustrated in Fig. 1, which plots measured moment loads acting on two perpendicular directions from an OWT installed in the North Sea [10]. Although some first attempts have been done to include this effect [8], these efforts have been limited to $p-y$ curves. In order to incorporate multidirectional coupling in foundation models outside the $p-y$ curves approach, more studies investigating coupling during multidirectional loading are needed.

Some authors have investigated experimentally or numerically the effect of multidirectional loading on the response of piles [11, 12, 13, 14, 15, 16]. Most of the experimental studies focused on earthquake loads [12, 13, 15], which are generally larger than loads acting on OWTs, or on the response of flexible piles [11], which differs from the semi-rigid monopile behaviour. Rudolph et al. [14] and Sheil and McCabe [16] investigated the response of a monopile in sand experimentally and numerically, respectively. Nevertheless, they focused on the accumulated displacements rather than on the load-displacement response, which controls the foundation stiffness and damping, and therefore the OWT system characteristics. On this regard, there is still need for multidirectional loading studies that can be directly employed to verify and support extensions of foundation models for integrated analyses of OWTs.

This paper investigates numerically the response of monopiles to multidirectional loading, with focus on the load-displacement response, and proposes an extension of the foundation model for integrated analyses of OWTs described in Page et al. [9]. The paper is structured as follows. Section 2 describes

and validates the constitutive soil model employed in the numerical analyses. Then, Section 3 describes the multidirectional loading analyses of a monopile, and displays the results. This is followed by Section 4, which presents the formulation of a foundation macro-element model for integrated analyses of OWTs, which has been extended to account for the effects of multidirectional loading. Finally, Section 5 discusses the results and highlights the limitations of the foundation model, and Section 6 outlines the conclusions.

2. Characterisation of the multidirectional cyclic loading behaviour in clay

2.1. Introduction

During multidirectional loading of offshore wind turbines, the principal stress components of the soil around the pile may vary cyclically. In order to investigate numerically the effects of multidirectional loading, a constitutive soil model capable of reproducing 3D stress conditions in time-domain simulations is needed. The model has to be realistic enough to represent soil behaviour, and at the same time simple enough to allow for implementation in a commercial 3D FE software. Focus is set on pile foundations embedded in cohesive soils subjected to cyclic loading under undrained conditions, that is, with no volume change.

There exist several constitutive models that can model cyclic loading in clay under undrained conditions in time-domain simulations. Most of them can be placed into one of the two main families: bounding surface plasticity [17, 18] and multisurface plasticity [19, 20].

In *bounding surface plasticity models*, the plastic deformation depends on the distance between the current stress and an "image" stress on the bounding surface, and the hardening is defined by a predefined continuous function. This has the advantage that it can easily model the non-linear stress-strain behaviour observed at low strain levels, however it makes the model calibration less flexible. In addition, bounding surface plasticity models do not follow Masing's rule [21] and may accumulate strains, that is, they may show ratcheting.

In *multisurface plasticity models*, the plastic deformation depends on how a family of nested surfaces move in the stress space, and the hardening is defined by piece-wise linear curves. These models have the advantage that they are conceptually simple, easy to implement, and allow for flexible calibrations. In addition, some model formulations do not accumulate strains [22], that is, they produce closed loops.

For this study, multisurface plasticity has been chosen because it produces closed loops, which are expected at the relatively low cyclic load levels (compared to the pile capacity) and for the number of cycles present in the 10 to 60 min time windows considered in integrated load simulations of OWT. In addition, a simpler implementation and a more flexible calibration is foreseen.

In the following sections, we describe a simple total stress-based model that can reproduce cyclic loading under undrained conditions of clays in time-domain simulations, together with its implementation

in the commercial software PLAXIS 3D and a comparison against true triaxial tests in clay under constant mean stress.

2.2. A simple constitutive model for cyclic loading under undrained conditions of clays

2.2.1. Overview

The total stress-based constitutive model is formulated as a multi-surface plasticity model. The cyclic behaviour is modelled through kinematic hardening, and follows Masing's behaviour in uniaxial or unidirectional predictions. The model is a total stress model, which means that it cannot predict pore-pressure build up due to change in effective mean stresses. The model formulation is based on the formulation presented in Iwan [20], Montáns [23] and in Grimstad et al. [24], and summarised in Section 2.2.2.

2.2.2. Model formulation

If the stress state is characterised by the tensor $\boldsymbol{\sigma}$, and the corresponding strain tensor is $\boldsymbol{\epsilon}$, the constitutive relation between an infinitesimal increment in stress $d\boldsymbol{\sigma}$ and the corresponding infinitesimal increment in strain $d\boldsymbol{\epsilon}$ can be established from the following basic components: (1) a principle of adding the elastic and the plastic contributions; (2) a relationship that governs the elastic response, based on Hooke's law; and (3) ingredients controlling the plastic contribution, which are the yield criterion, the flow rule, the hardening law and a consistency condition. These ingredients are specified in the following paragraphs.

Yield criterion. The yielding of clays during loading under undrained conditions is independent of the total mean stress, and the yield criterion can be defined with only deviatoric stresses. From the different yield criteria described only by deviatoric stresses, the Von Mises criterion [25] displayed in Eq. 1 is defined by a smooth function that can be easily implemented, and thus it is selected.

$$f_i(\boldsymbol{\sigma}, \boldsymbol{\alpha}_i) = \sqrt{3 \cdot J_2(\boldsymbol{\sigma}, \boldsymbol{\alpha}_i)} - r_i = 0 \tag{1}$$

Where J_2 is the second invariant of the deviatoric stress tensor, which is function of the deviatoric stress tensor $\boldsymbol{\sigma}$ and the back-stress $\boldsymbol{\alpha}_i$. The Von Mises yield criterion is visualised as a circle in the π-plane, as illustrated in Fig. 3. The back-stress $\boldsymbol{\alpha}_i$ defines the center and r_i the radius of each circle. The innermost circle (for $i = 1$) separates the elastic from the elasto-plastic region.

Flow rule. The associative flow rule defined in Eq. 2, is employed.

$$d\boldsymbol{\epsilon}_{\boldsymbol{i}}^{p} = d\lambda_i \cdot \frac{\partial f_i}{\partial \boldsymbol{\sigma}} \tag{2}$$

Where $d\lambda_i$ is the plastic multiplier, an scalar that determines the magnitude of $d\boldsymbol{\epsilon}_{\boldsymbol{i}}^p$. The total plastic strain, $d\boldsymbol{\epsilon}^p$, is computed as the sum of the plastic contributions of the active yield surfaces assuming Koiter's rule [26].

Hardening law. The multi-surface plasticity model presented here is of the pure kinematic hardening type, where the yield surfaces do not change in size but only translate in the stress space. The kinematic hardening rule defines the direction of $d\boldsymbol{\alpha}_i$, that is, how do the centre of each yield surface translate. The kinematic hardening rule proposed by Grimstad et al. [24], shown in Eq. 3, has been adopted for each yield surface.

$$d\boldsymbol{\alpha}_i = \boldsymbol{D}_i^p \cdot d\boldsymbol{\epsilon}^p = d\lambda_i \cdot \boldsymbol{D}_i^p \cdot \frac{\partial f_i}{\partial \boldsymbol{\sigma}} \tag{3}$$

Where $\boldsymbol{D}_i^p$ is the plastic stiffness matrix defined in Eq. 4:

$$\boldsymbol{D}_i^p = \begin{bmatrix} \frac{4}{3}G_i^p & -\frac{2}{3}G_i^p & -\frac{2}{3}G_i^p & 0 & 0 & 0 \\ -\frac{2}{3}G_i^p & \frac{4}{3}G_i^p & -\frac{2}{3}G_i^p & 0 & 0 & 0 \\ -\frac{2}{3}G_i^p & -\frac{2}{3}G_i^p & \frac{4}{3}G_i^p & 0 & 0 & 0 \\ 0 & 0 & 0 & G_i^p & 0 & 0 \\ 0 & 0 & 0 & 0 & G_i^p & 0 \\ 0 & 0 & 0 & 0 & 0 & G_i^p \end{bmatrix} \tag{4}$$

Where G_i^p is the plastic shear modulus associated to each of the yield surfaces. In a 1D kinematic hardening model, see for instance Iwan [20], G_i^p is the stiffness of each spring-slider system. The matrix $\boldsymbol{D}_i^p$ is interpreted as a ratio between $(\boldsymbol{\sigma} - \boldsymbol{\alpha}_i)$ and $d\boldsymbol{\epsilon}^p$. For each yield surface i, the plastic stiffness matrix $\boldsymbol{D}_i^p$, is constant, which leads to piece-wise linear hardening curves.

Note that the kinematic hardening rule is only formulated in terms of $\boldsymbol{\sigma}$ and $\boldsymbol{\alpha}_i$, not in terms of other surfaces. There is not a non-intersection condition or a consistency equation to avoid intersection of yield surfaces, as prescribed by other authors, see for instance [19]. The main consequence of allowing the yield surfaces to intersect is that instead of having a bi-linear relation between two surfaces, a multilinear relation might be produced [27]. Puzrin and Houlsby [27] argue that this is not generally a problem and it often helps simplifying the model implementation. In addition, Montáns and Caminero [22] showed that the use of Mrôz [19] kinematic hardening rule (where the translation of the surfaces satisfies a non-intersection condition) in multiaxial predictions had some issues. First, the multi-surface plasticity model response depended on the number of yield surfaces used in the calibration. And second, Mrôz's kinematic hardening rule lead to uncontrolled multiaxial ratcheting, while the uniaxial response did not show ratcheting. In that sense, the kinematic hardening rule from Eq. 3 does not depend on the number of surfaces and does not predict multiaxial ratcheting, which is more consistent with the uniaxial behaviour.

Consistency condition. In addition to the yield criterion, the flow rule and the kinematic hardening rule, the consistency condition is needed to find $d\lambda_i$ of each yield surface. If j yield surfaces are active, then the consistency condition can be expressed as:

$$\boldsymbol{f} = \begin{bmatrix} f_1 \\ f_2 \\ \vdots \\ f_j \end{bmatrix} \approx \begin{bmatrix} a_{11} + A_1 & a_{12} & \dots & a_{1j} \\ a_{21} & a_{22} + A_2 & \dots & a_{2j} \\ \vdots & \vdots & \ddots & \vdots \\ a_{j1} & a_{j2} & \dots & a_{jj} + A_j \end{bmatrix} \cdot \begin{bmatrix} d\lambda_1 \\ d\lambda_2 \\ \vdots \\ d\lambda_j \end{bmatrix} = \boldsymbol{\Xi} \cdot d\boldsymbol{\lambda} \tag{5}$$

Where

$$a_{ik} = \left(\frac{\partial f_i}{\partial \boldsymbol{\sigma}}\right)^T \cdot \boldsymbol{D} \cdot \left(\frac{\partial f_k}{\partial \boldsymbol{\sigma}}\right) \tag{6}$$

And

$$A_k = \left(\frac{\partial f_k}{\partial \boldsymbol{\sigma}}\right)^T \cdot \boldsymbol{D}_k^p \cdot \left(\frac{\partial f_k}{\partial \boldsymbol{\sigma}}\right) \tag{7}$$

Note that in Eq. 6 and 7, the associativity of the flow rule has been included.

2.2.3. Numerical Implementation

The constitutive model described in Section 2.2.2 has been implemented as a user defined soil model in the commercial software PLAXIS 3D [28]. The implementation follows an explicit algorithm with correction. An implicit algorithm for the same model formulation can be found in Montáns [23]. In each increment, that is, from step n to step $n+1$, the incremental strain $\Delta\boldsymbol{\epsilon}$ is given as input, and we seek to determine the updated stress state $\boldsymbol{\sigma}_{n+1}$ and the updated state variables, in this case the back-stress $\boldsymbol{\alpha}_{i,n+1}$ of each yield surface i.

The calculation is started by computing the trial stress $\boldsymbol{\sigma}_{n+1}^{tr}$ as $= \boldsymbol{\sigma}_n + \boldsymbol{D} \cdot \Delta\boldsymbol{\epsilon}$ and the trial back-stress $\boldsymbol{\alpha}_{i,n+1}^{tr}$ as $\boldsymbol{\alpha}_{i,n}$. Before proceeding with the algorithm, we need to determine if yield surface i is active for $\boldsymbol{\sigma}_{n+1}^{tr}$ and $\boldsymbol{\alpha}_{i,n+1}^{tr}$ by checking if $f_{i,n+1} \geq 0$. If yield surface i is active, then the yield criterion presented in Eq. 1 has to be satisfied at the end of the step, that is $f_{i,n+1} = 0$.

Combining the associative flow rule, the decomposition of the strain into an elastic and a plastic part, and Koiter's rule, $\boldsymbol{\sigma}_{n+1}$ can be calculated as:

$$\boldsymbol{\sigma}_{n+1} = \boldsymbol{\sigma}_{n+1}^{tr} - \boldsymbol{D} \cdot \sum_{j=1}^{i} \Delta\lambda_j \cdot \left\{\frac{\partial f_j}{\partial \boldsymbol{\sigma}}\right\}_{n+1} \tag{8}$$

Where i is the number of active surfaces. In order to make the algorithm efficient, it is assumed that if one yield surface is active, all the surfaces enclosed by j, that is, from 1 to j, are also active. On the other hand, if yield surface j is not active, the surfaces disclosed by surface j, that is, from $j+1$, are not

checked and it is assumed that they are not active. From the translation rule:

$$\boldsymbol{\alpha}_{i,n+1} = \boldsymbol{\alpha}_{i,n} + \Delta\lambda_i \cdot \boldsymbol{D}_i^p \cdot \left\{ \frac{\partial f_i}{\partial \boldsymbol{\sigma}} \right\}_{n+1} \tag{9}$$

The plastic multiplier is calculated iterating until

$$\sum_{j=1}^{i} |f_{j,n+1}| < tol \cdot s_u \tag{10}$$

Where i is the number of active surfaces and tol is a tolerance specified by the user as an input parameter. In every iteration, $\Delta\boldsymbol{\lambda}$, the vector containing the $\Delta\lambda_i$, is updated by adding $\delta\Delta\boldsymbol{\lambda}$, which is computed as:

$$\delta\Delta\boldsymbol{\lambda} = \boldsymbol{\Xi}_{n+1}^{-1} \cdot \boldsymbol{f}_{n+1} \tag{11}$$

Where $\boldsymbol{f}_{n+1}$ is a vector containing $f_{j,n+1}$. Note that $\delta\Delta\boldsymbol{\lambda}$ can have both positive and negative terms. Generally less than three iterations are needed to reach convergence. If the model does not converge after a certain number of iterations defined by the user, sub-stepping is automatically called in. Every time sub-stepping is activated, the input incremental strain $\Delta\boldsymbol{\epsilon}$ is divided into ten equal parts.

2.2.4. Model calibration

The parameters required to calibrate the constitutive model are:

- the ratio between the maximum shear modulus and the undrained shear strength of the soil G_{max}/s_u,
- the undrained shear strength of the soil s_u,
- Poisson ratio ν, and
- a normalised shear stress - shear strain curve extracted, for instance, from laboratory tests, that provides the more representative stress path for the problem of interest. The choice of the most representative test will depend on the type of loading (static or cyclic) and the representative stress paths for the given boundary value problem. Since the model does not account for anisotropic behaviour, it may also be necessary to use different input data in different zones of the boundary value problem.

In addition, the number of yield surfaces, the tolerance and the number of iterations before sub-stepping is called in can be given as input. From this input, the required plastic model parameters r_i and G_i^p are derived assuming that the yield surfaces are coupled in series.

The initial position of the yield surfaces is set at the origin, assuming $K_0 = 1$.

2.2.5. Model assessment

The adequacy of the model to simulate multiaxial loading under undrained conditions is assessed by comparing experimental data and simulations. The experimental data correspond to the drained cyclic true triaxial test under constant mean stress described in Nakai [29]. The test was carried out on normally consolidated Fujinomori clay under constant mean stress to examine the effect of a change in direction of the shear stress and/or the principal stress during cyclic loading [29]. The stress path describes the shape of a bow tie on the octahedral or π-plane, as illustrated in Fig. 2. The applied stresses at the end of each path are listed in Table 1. Note that in Fig. 2 the volumetric strain has been subtracted from the original drained test data in order to be able to compare the constant mean stress experimental results with the undrained model.

Table 1: Applied stress paths in the comparison with the cyclic true triaxial test under constant mean stress described in Nakai [29].

	O	A	B	O	C	D	O	E
σ_x [kPa]	-98	-58.8	-42	-98	-176.4	-126	-98	-49
σ_y [kPa]	-98	-176.4	-126	-98	-58.8	-42	-98	-49
σ_z [kPa]	-98	-58.8	-126	-98	-58.8	-126	-98	-196
σ_1/σ_3 [-]	1	3	3	1	3	3	1	4

The numerical simulations are performed with the constitutive model described in Section 2.2.2. The model is calibrated to the stress-strain curve displayed in Fig. 2 between points O and A. The calibrated parameters for the consititutive model are listed in Table 2 and Table 3.

Table 2: Calibrated soil parameters for the cyclic true triaxial test under constant mean stress described in Nakai [29].

G_{max}/s_u	ν	s_u	Number of yield surfaces	tol	Max number of iterations
[−]	[−]	kPa	[−]	[−]	[−]
125	0.495	85	8	10^{-5}	10

Table 3: Calibrated normalised plastic stiffness, G_i^p/s_u, and yield limits, r_i/s_u, for the cyclic true triaxial test under constant mean stress described in Nakai [29].

G_i^p/s_u	[−]	119	53	40	26	16	8	4	0
r_i/s_u	[−]	0.22	0.42	0.60	0.74	0.85	0.92	0.97	1.00

The comparison between the experiment and the simulation indicates that, despite its simplicity, the constitutive model describes quite well the cyclic behaviour of undrained clay under three different principal stresses. For this particular true triaxial test, the agreement between the model and the experimental data is similar to the agreement between the subloading t_{ij} model described in Nakai [29] and the same

experimental data. In particular, the comparison shows that:

- From O to A, good agreement is found in the three deviatoric strain directions. This can be expected since the model is calibrated to this part of the test. Note that in this part of the test, σ_y is increased while σ_x and σ_z are reduced equally.

- In the path $A-B-C-D-O$, a fair agreement is found in the three strain directions, specially at low strain levels. Note that the shift between the simulations and measurements is due to an slight underprediction of $\epsilon_x - 1/3\epsilon_v$ in A to B and of $\epsilon_y - 1/3\epsilon_v$ in O to A. This disagreement may be because the constitutive model is formulated as an isotropic model with a Von Mises yield criterion. Natural clays (like the Fujinomori clay employed in the true triaxial test) are anisotropic materials, and they exhibit different behaviour in extension and compression. In that sense, the isotropic constitutive model with Von Mises yield surfaces simulates the same behaviour in extension and compression paths, both during monotonic loading as well as during unloading and reloading.

- From O to E, a fair agreement is found in $\epsilon_y - 1/3\epsilon_v$, while the simulations overpredict $\epsilon_x - 1/3\epsilon_v$ and $\epsilon_z - 1/3\epsilon_v$. This can be partially explained by analysing Fig. 3c. As the stress point starts moving from O to E, three yield surfaces are activated almost at the same time, which leads to a softer response, while a more gradual activation of yield surfaces could have been expected. Also note that there is a small gap in the simulated response around O. This is a consequence of the model implementation, which assumes that if one surface is inactive, all the surfaces unenclosed by it are also inactive.

3. Characterisation of multidirectional loading behaviour at foundation level

3.1. Introduction

The characterisation of the foundation behaviour under multidirectional loading was carried out through numerical analyses of a pile foundation embedded in a soil volume. The simulations were performed with the commercial 3D Finite Element Analyses code PLAXIS [28]. For the soil modelling, the consitituve model described in Section 2 was employed.

3.2. Sign convection and nomenclature

In the simulations, different combinations of the horizontal forces H_x and H_y, and of the moments M_x and M_y in the x- and y- directions, were applied at the centre of the pile head's cross-section. Fig. 4 presents the notation for the positive pile head loads and displacements, which follows the sign convection suggested by Butterfield et al. [30].

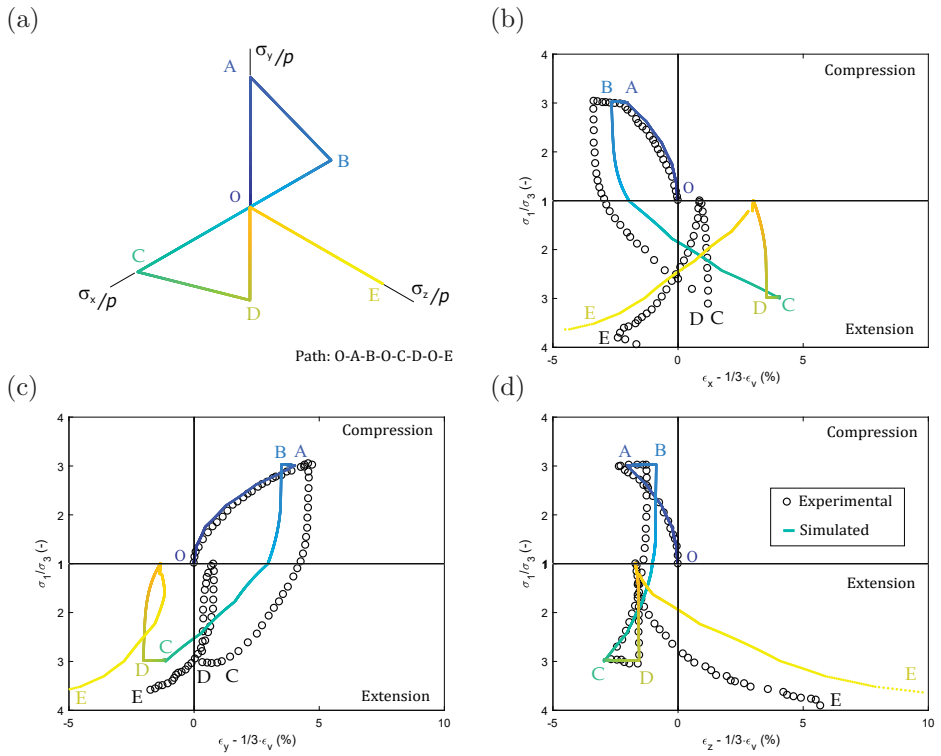

Figure 2: Comparison of the total-stress constitutive model for cyclic loading and the cyclic true triaxial test under constant mean stress described in Nakai [29]. Note that the volumetric strain has been subtracted from the original drained test data.

It is often convenient to write the loads as a generalised load vector $\boldsymbol{t}$, and the displacements as the work conjugate generalised displacement vector $\boldsymbol{v}$, as described by Eq. 12.

$$\boldsymbol{t} = \begin{bmatrix} H_y \\ H_x \\ M_y/D \\ M_x/D \end{bmatrix}; \quad \boldsymbol{v} = \begin{bmatrix} u_y \\ u_x \\ D \cdot \theta_y \\ D \cdot \theta_x \end{bmatrix} \tag{12}$$

Where D is the pile diameter.

3.3. Numerical modelling aspects

The pile was modelled as a solid volume with an equivalent stiffness that reproduces the bending stiffness of the hollow pile, neglecting the stiffness of the soil plug. Pile installation effects were not considered, and the pile was modelled as 'wished in place' in the center of the soil volume. The contact between the soil and the pile was modelled by interface elements with a no-tension criterion that allowed gap opening and gap closure between the soil and the pile.

The soil domain was modelled as a cylinder with a radius of 12.5 pile diameters, and a height of 6.5 pile diameters. Boundary conditions were applied at the base of the model and at the vertical boundaries. The three displacements components in the three coordinate directions were set to zero at bottom boundary.

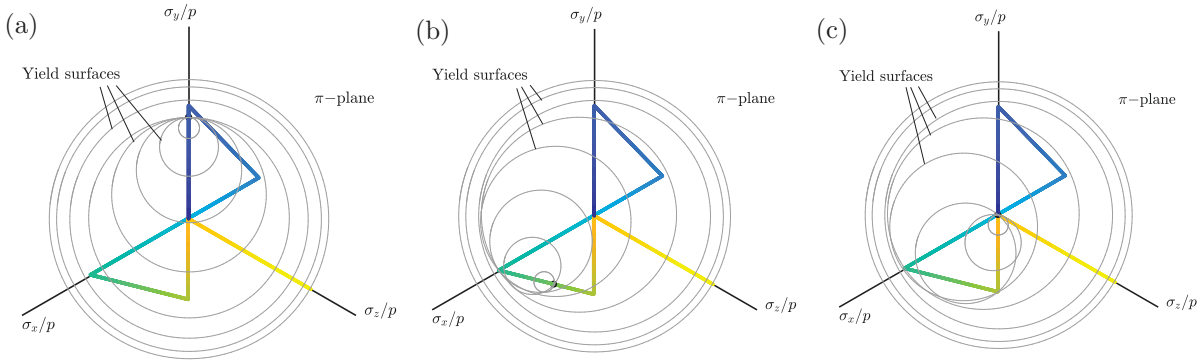

Figure 3: Visualisation of the yield surfaces of the constitutive model in the π-plane: (a) reaching point A; (b) between points C and D; and (c) at point O, towards point E.

(a) Force components.

(b) Displacements components.

Figure 4: Nomenclature of the positive forces and displacement components for lateral loading. Sign conventions according to Butterfield et al. [30].

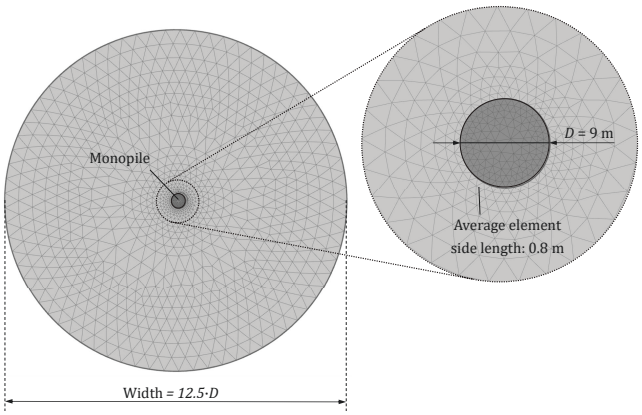

Figure 5: Plan view of the model dimensions and mesh refinement.

On the vertical boundaries, the normal component was fixed.

The finite element mesh employed in the numerical analyses is shown in Fig. 5, together with the model dimensions. The mesh had roughly 145 000 10-noded tetrahedral soil elements with an average element side length of 4.4 m. The mesh was refined around the pile, where an average element side length of 0.8 m was used. A mesh sensitivity study was carried out to ensure that the mesh discretisation did not affect the load-displacement response of the pile.

3.4. Case study

3.4.1. Overview

The case study is based on the WAS-XL monopile in clay [31], a reference design for large diameter monopile foundations. The WAS-XL monopile was designed to support the DTU 10 MW OWT [32], and the soil conditions, pile dimensions and applied loads are considered to be representative for typical offshore wind sites [31].

3.4.2. Soil properties

The soil considered is an idealised homogeneous stiff clay with a plasticity index of 30% and a over-consolidation ratio of 4. Fig. 6 illustrates the undrained shear strength and maximum shear modulus of the soil with depth. A constant ratio between the undrained shear strength and the initial effective vertical stress, $s_u/\sigma'_{v0} = 1$ was selected based on correlations from Andersen [33].

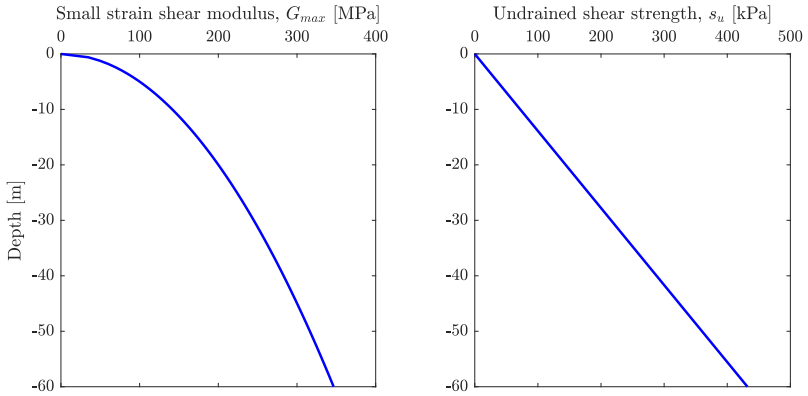

Figure 6: Idealised small strain shear modulus and undrained shear strength with depth employed in the case study, modified after [31].

3.4.3. Foundation dimensions

The pile considered is a tubular steel pile with a diameter $D = 9$ m and a constant pile wall thickness $t = 0.1125$ m, embedded $L = 36$ m into the soil. This leads to a length-to-diameter ratio of $L/D = 4$ and a diameter-to-wall thickness of $D/t = 80$, which is representative for monopiles supporting OWTs. For the steel, a Young modulus of $E = 210$ GPa and a Poisson ratio of $\nu = 0.3$ were assumed.

3.4.4. Loading conditions

Table 4 lists the magnitude and type of simulated loads. Initially, idealised load paths were applied to illustrate the effect of multidirectional loading on the simulated response. Both monotonic and cyclic load paths were tested. Then, load histories from the DTU 10 MW OWT on a monopile foundation were applied. The load histories correspond to an ULS storm condition, with an average wind speed of 38.5 m/s, a significant wave height of 9.5 m, and a peak wave period of 12.3 s [31].

Table 4: Simulated load paths

Load path type		Load range			
Nature	Shape	H_y [MN]	H_x [MN]	M_y [MNm]	M_x [MNm]
Monotonic	Radial*	10	0	300	0
Cyclic	Rectangular*	10	10	0	0
	Bow tie*	10	0	100	0
	From OWT simulations	-0.5 to 0.5	-2 to 3.5	-40 to 130	-54 to 45
		-0.6 to 0.6	-6 to 12	-300 to 300	-54 to 68

*Idealised

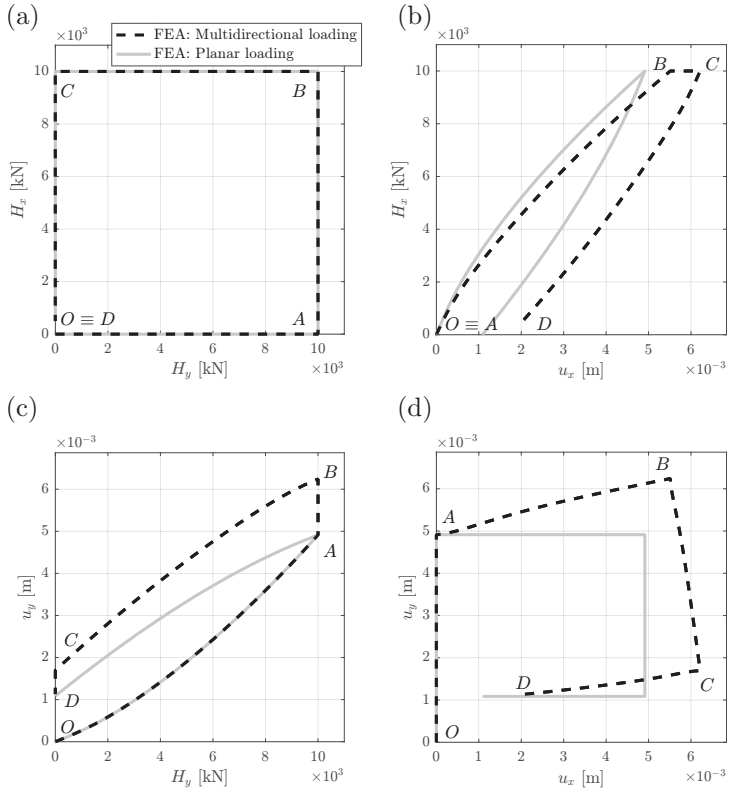

Figure 7: Comparison between FEA simulations with $H_y - H_x$ considering multidirectional or planar conditions.

3.5. Simulated behaviour at foundation level

The simulated behaviour at foundation level is evaluated by analysing the force-displacement relations at the pile head, computed by finite element analyses assuming planar and multidirectional loading conditions. In the planar loading conditions, the loads in the $x-$ and $y-$ directions are applied uncoupled in two separate finite element analyses. In the multidirectional loading conditions, the loads are applied coupled in the same finite element analysis. Figs. 7 and 8 show the relation between the forces and the simulated displacements for rectangular load paths.

Results from multidirectional loading indicate that there is a coupling between the response computed in two perpendicular loading planes. In particular, the following is observed in Fig. 7 while comparing

the response of two horizontal loads in the $x-$ and $y-$ directions:

- When only one load component is applied (e.g. H_y from O to A in Fig. 7c), the same displacement is computed under multidirectional and planar loading conditions. Note that the load-displacement response is non-linear, which indicates that both elastic and plastic displacements are generated.

- However, the behaviour changes when a second load component is increased from zero while the first load component is kept constant (e.g. H_x from A to B in Fig. 7b). Under these load conditions, the planar response is a displacement path parallel to the $x-$axis (see Fig. 7d). The results from multidirectional loading presented in Fig. 7d show that u_x increases more due to a constant H_y, and that u_y increases with H_x. Note that the $H_x - u_x$ plastic response between A and B (displayed in Fig. 7b) is softer than the planar response, which is equal to the $H_y - u_y$ response between O and A in Fig. 7c.

- The coupling is also observed during unloading, see for instance path B to C in Fig. 7b.

- The elastic response is the same for multidirectional and planar loading conditions. This can be observed in the load-displacement response, by looking at the initial stiffness in Fig. 7b, and in the displacement plane in Fig. 7d, where every time there is a change in loading direction, the displacement path (e.g. $u_x - u_y$) starts parallel to the load path.

The same observations can be made for Fig. 8, where the response to a horizontal load H_y and a moment acting on the perpendicular plane, M_y, are displayed.

In the results presented above, the total or elasto-plastic displacement is shown. The elasto-plastic displacement can be decomposed into the sum of an elastic and a plastic part. The elastic response does not seem to be affected by the multidirectionality, however, the plastic response is. While trying to analyse how the plastic displacements are generated as a function of the applied loads, it might be convenient to look at how the plastic work evolves. The plastic work W^p can be calculated as:

$$W^p = \int_0^{u_y^p} H_y \cdot du_y^p + \int_0^{u_x^p} H_x \cdot du_x^p + \int_0^{\theta_y^p} M_y \cdot d\theta_x^p + \int_0^{\theta_x^p} M_x \cdot d\theta_x^p \tag{13}$$

The contours of constant plastic work computed from the radial loads paths listed in Table 4 are shown in Fig. 9 in the $M_y/D - H_x$ and $M_y/D - H_y$ planes. The shape of the contours in the $M_y/D - H_x$ plane can be approximated by a rotated ellipse, as illustrated in Fig. 9a. This is consistent with the results from FEA presented in Page et al. [9]. In the $M_y/D - H_y$ plane, shown in Fig. 9b, the contours of plastic work can be approximated by a non-rotated ellipse.

In addition, Fig. 10 plots the direction of the incremental plastic displacement vectors computed from

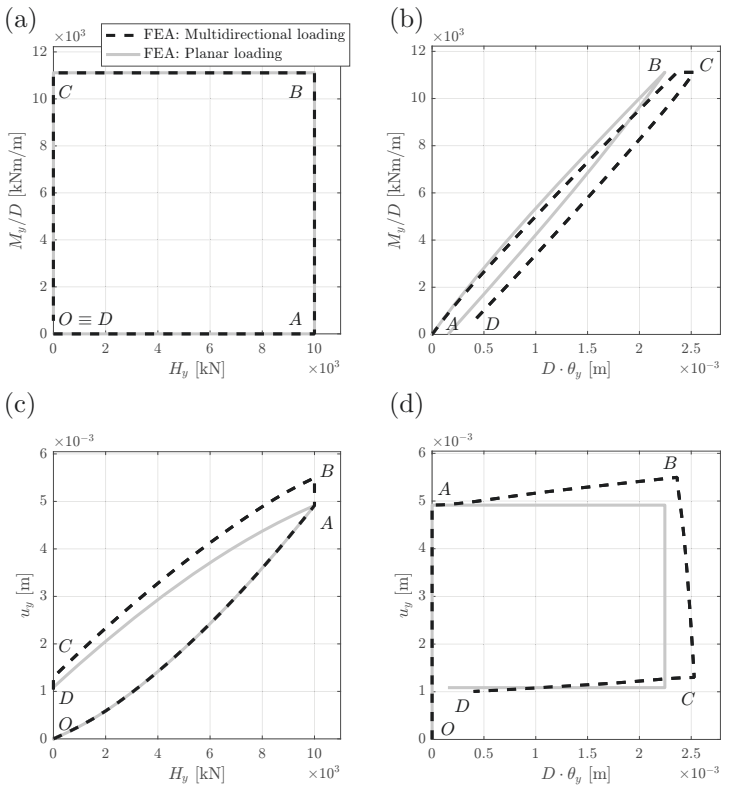

Figure 8: Comparison between FEA simulations with $H_y - M_y/D$ considering multidirectional or planar conditions. Note that the rotation angle θ is calculated as the secant value assuming that the pile head's cross-section is infinitely stiff in the finite element model.

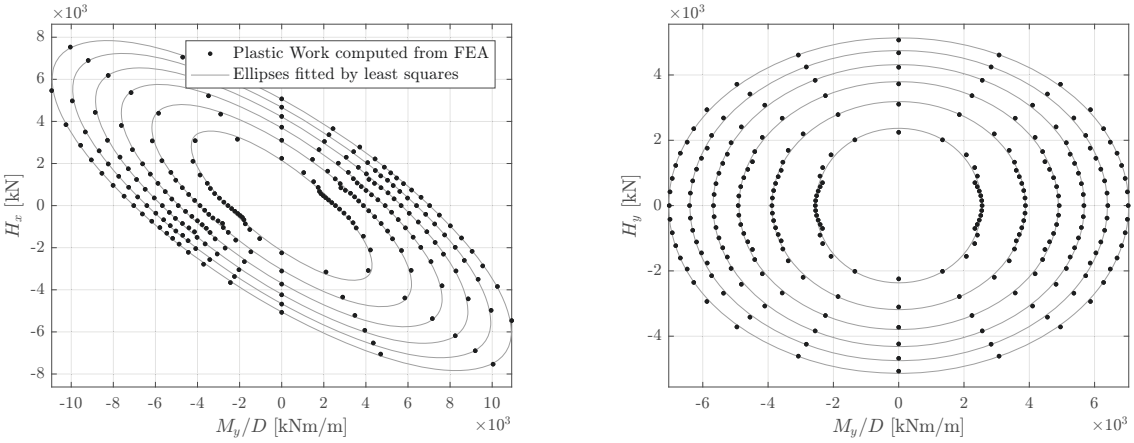

(a) In $M_y/D - H_x$ plane for $H_y = M_x/D = 0$

(b) In $M_y/D - H_y$ plane for $H_x = M_x/D = 0$

Figure 9: Contours of constant plastic work computed from FEA by applying radial paths.

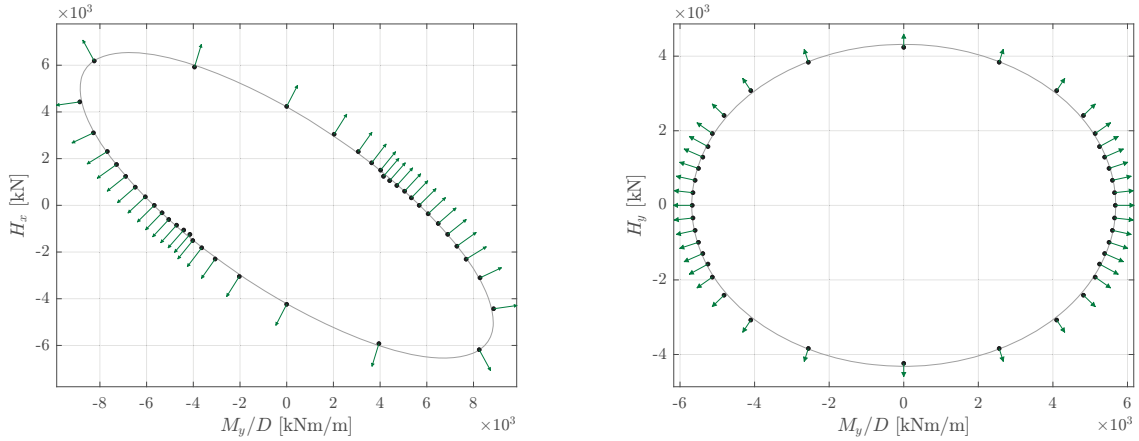

(a) In $M_y/D - H_x$ plane for $H_y = M_x/D = 0$ (b) In $M_y/D - H_y$ plane for $H_x = M_x/D = 0$

Figure 10: Direction of the incremental plastic displacement vector computed from FEA by applying radial paths.

FEA, which are perpendicular to the plastic work contours. This is convenient as the direction of the incremental plastic displacement vectors could be expressed as the gradient of the plastic work contours. Based on these findings, the pile macro-element model presented in Page et al. [9] has been extended to account for multidirectional cyclic lateral loading.

4. A macro-element model for multidirectional lateral loading of piles

4.1. Model formulation

The macro-element for multidirectional lateral loading of piles is formulated as a multi-surface plasticity model with kinematic hardening, as the soil model described in Section 2.2. The macro-element model relates the generalised load $\boldsymbol{t}$ and the generalised displacement $\boldsymbol{v}$ at the pile head. Note that $\boldsymbol{t}$ and $\boldsymbol{v}$ are defined in Eq. 12 and their components are sketched in Fig. 4. The constitutive relation is established assuming that the generalised displacement increment $d\boldsymbol{v}$ can be decomposed into the sum of elastic ($d\boldsymbol{v}^e$) and plastic ($d\boldsymbol{v}^p$) components.

4.1.1. Elastic response

The generalised elastic displacement increment $d\boldsymbol{v}^e$ is related to the generalised load increment $d\boldsymbol{t}$ through an elastic stiffness matrix $\boldsymbol{K}$. The coefficients of $\boldsymbol{K}$ depend on the pile dimensions, pile properties, soil layering and soil properties and drainage conditions.

4.1.2. Yield criterion and loading surfaces

The yield criterion f determines the yielding state of the material, and it can be represented in the generalised forces space as yield surfaces. The yield surfaces in the macro-element adopt the elliptical shape of the contours of plastic work computed in Section 3.5 and illustrated in Fig. 9. Choosing

the contours of constant plastic work as yield surfaces has some advantages. First, it simplifies the model implementation, since an associative flow rule can be selected. In addition, it guarantees that all components of plastic displacements are considered in the flow rule and the hardening law. Bienen et al. [34] performed small-scale tests on a shallow foundation on sand, and concluded that the hardening law had to include radial hardening components, that is, horizontal displacements and rotations, to match experimental results. In this sense, the yield surfaces defined as contours of constant plastic work lead to an associative flow rule and hardening law that include all radial displacement components.

Based on this, the yield criterion f_i of surface i is formulated as a quadratic form defined as:

$$\begin{aligned} f_i(\boldsymbol{t}, \boldsymbol{\alpha}_i) = & \\ & a_{1,i} \cdot (H_x - \alpha_{H_x,i})^2 + + a_{1,i} \cdot (H_y - \alpha_{H_y,i})^2 + a_{2,i} \cdot (M_y/D - \alpha_{M_y,i})^2 \\ & + a_{2,i} \cdot (M_x/D - \alpha_{M_x,i})^2 + 2 \cdot a_{3,i} \cdot (H_x - \alpha_{H_x,i}) \cdot (M_y/D - \alpha_{M_y,i}) \\ & - 2 \cdot a_3 \cdot (H_y - \alpha_{H_y,i}) \cdot (M_x/D - \alpha_{M_x,i}) - 1 = 0 \end{aligned} \tag{14}$$

Where

- $\boldsymbol{\alpha}_i$ are the generalised state variables or the coordinates of the back-stress vector of surface i. They define the position of the centre of the yield surface in the load space.
- $a_{1,i}$, $a_{2,i}$ and $a_{3,i}$ describe the size and the orientation of yield surface i. Due to symmetry, the same coefficients are applied in the $x-$ and $y-$ directions. Note that in Fig. 9 the orientation and the ratio between the major and minor axes are approximately constant for all computed contours of plastic work. In the model formulation, the ratio between the minor and major axes, s, and the orientation defined by β in Fig. 9a are assumed to be constant for all the yield surfaces. This implies that the yield surfaces are homothetic to each other.

This yield criterion is an extension of the yield criterion presented in Page et al. [9] for planar conditions, and it is comparable to the elliptical yield criterion proposed by Martin [35] and Bienen et al. [34] for a shallow foundation in sand subjected to 6 degrees-of-freedom loading.

4.1.3. Flow rule

The flow rule defines the direction of the generalised plastic displacement increment $d\boldsymbol{v}^p$. Fig. 10 showed that the direction of the $d\boldsymbol{v}^p$ computed from FEA was perpendicular to the contours of plastic work. Since the later are adopted as loading or yield surfaces, an associative flow rule can be employed for each yield surface i. The $d\boldsymbol{v}^p$ is computed as the sum of the plastic contributions of the active yield surfaces assuming Koiter's rule [26]:

$$d\boldsymbol{v}^p = \sum_{i=1}^{j} d\boldsymbol{v}_i^p = \sum_{i=1}^{j} d\lambda_i \cdot \frac{\partial f_i}{\partial \boldsymbol{t}} \tag{15}$$

Where $d\lambda_i$ is an scalar that determines the magnitude of $d\boldsymbol{v}_i^p$ and j is the number of active or yielding surfaces, that is, surfaces that are translating in the load space.

4.1.4. Hardening law

The kinematic hardening rule defines the direction of $d\boldsymbol{\alpha}_i$, that is, how does the centre of each yield surface i translate. In the macro-element model, the kinematic hardening rule employed in Grimstad et al. [24], and displayed in Eq. 16 has been adopted for each yield surface.

$$d\boldsymbol{\alpha}_i = \boldsymbol{K}_i^p \cdot d\boldsymbol{v}^p = d\lambda_i \cdot \boldsymbol{K}_i^p \cdot \frac{\partial f_i}{\partial \boldsymbol{t}} \tag{16}$$

Where $d\lambda_i$, which defines the size of $d\boldsymbol{v}^p$ in the flow rule. Note that the plastic stiffness matrix $\boldsymbol{K}_i^p$ is interpreted as a ratio between $(\boldsymbol{t} - \boldsymbol{\alpha}_i)$ and $d\boldsymbol{v}^p$. For each yield surface i, the plastic stiffness matrix $\boldsymbol{K}_i^p$, is constant, which leads to piece-wise linear hardening curves.

4.1.5. Consistency condition

If the macro-element model has j active yield surfaces, the consistency condition can be expressed as in Eq. 5, where

$$a_{ik} = \left(\frac{\partial f_i}{\partial \boldsymbol{t}}\right)^T \cdot \boldsymbol{K} \cdot \left(\frac{\partial f_k}{\partial \boldsymbol{t}}\right) \tag{17}$$

And

$$A_k = \left(\frac{\partial f_k}{\partial \boldsymbol{t}}\right)^T \cdot \boldsymbol{K}_k^p \cdot \left(\frac{\partial f_k}{\partial \boldsymbol{t}}\right) \tag{18}$$

Note that Eqs. 17 and 18 are the same as Eqs. 6 and 7 in the constitutive soil model. The derivation of these equations is documented in detail in Skau et al. [36].

4.2. Numerical Implementation

The macro-element model has been implemented in the OWT simulation software *3DFloat* [37] and *SIMA* [38] via a *dll* (Dynamic Link Library) interface. In each iteration of a calculation step, that is, from step n to step $n+1$, OWT simulation software passes on an incremental generalised displacement ($\Delta\boldsymbol{v}$) to the foundation model, which transfers back the computed generalised force $\boldsymbol{t}_{n+1}$, and the updated state variables, in this case the back-stress $\boldsymbol{\alpha}_{i,n+1}$ for each yield surface i.

A change in the coordinate system is applied to simplify the macro-element model implementation and make it more robust in a similar manner as presented in Page et al. [9]. In this change, the axes in the load space $\boldsymbol{t}$ are transformed such as the 4D-ellipsoidal yield surfaces are displayed as 4D-spheres. Consequently, a yield criterion based on a single load invariant can be adopted and the implementation described in Section 2.2.3 can be directly employed. This is done through the linear transformation

matrix $\boldsymbol{R}$:

$$\boldsymbol{t}' = \boldsymbol{R} \cdot \boldsymbol{t} = \begin{bmatrix} \sin\beta & 0 & 0 & \cos\beta \\ 0 & -\sin\beta & \cos\beta & 0 \\ 0 & -s \cdot \cos\beta & -s \cdot \sin\beta & 0 \\ -s \cdot \cos\beta & 0 & 0 & s \cdot \sin\beta \end{bmatrix} \cdot \boldsymbol{t} \tag{19}$$

Where $\boldsymbol{t}'$ is the generalised load vector in the transformed axes system, s describes the squeezing of the elliptical yield surfaces and β describes its rotation. Note that this change can only be applied when all the yield surfaces are homothetic to each other. The parameters s and β are related to the ellipsoid parameters a_1/a_3 and a_2/a_3 as indicated in Eqs. 20 and 21.

$$\beta = \frac{\pi}{2} + \frac{1}{2} \cdot \arctan\left(\frac{2 \cdot a_1/a_3}{a_1/a_3 \cdot a_2/a_3 - 1}\right) \tag{20}$$

$$s = \left(\frac{a_1/a_3 \cdot a_2/a_3 + 1 - \sqrt{(a_1/a_3 \cdot a_2/a_3 - 1) \cdot (a_1/a_3 \cdot a_2/a_3 - 1 + 4 \cdot (a_1/a_3 \cdot a_2/a_3))}}{a_1/a_3 \cdot a_2/a_3 + 1 + \sqrt{(a_1/a_3 \cdot a_2/a_3 - 1) \cdot (a_1/a_3 \cdot a_2/a_3 - 1 + 4 \cdot (a_1/a_3 \cdot a_2/a_3))}}\right)^{1/2} \tag{21}$$

The incremental displacement $\Delta\boldsymbol{v}$ is transformed accordingly with the inverse of the transpose of $\boldsymbol{R}$, i.e. the $(\boldsymbol{R}^T)^{-1}$ matrix.

Before the constitutive equation is solved, $\Delta\boldsymbol{v}$ and the loads $\boldsymbol{t}_n$ are transferred into the transformed coordinate system by employing $\boldsymbol{R}$ and $(\boldsymbol{R}^T)^{-1}$. Then the constitutive relation is solved in the transformed axes system following the implementation described in Section 2.2.3 and the updated generalized forces are transformed back to the original coordinate system.

Note that the response to vertical and torsional loading has not been incorporated into the macro-element model formulation. The reason for this is that these two DOF and the lateral loading DOF are assumed to be uncoupled. However, in order to provide the foundation response in 6 DOF, the vertical and torsional DOF are modelled linear elastic in the *dll*. A linear elastic formulation is employed for the vertical and torsional DOF because, for monopile-based offshore wind turbines, the vertical and torsional cyclic loads are small, and therefore it is expected that the associated displacements and rotations can be approximated as linear.

4.3. Model calibration

The calibration of the multidirectional macro-element model is equal to the calibration of the planar macro-element described in Page et al. [9], where the user has to provide two types of input: (1) the coefficients of the elastic stiffness matrix and (2) load-displacement curves from non-linear analyses.

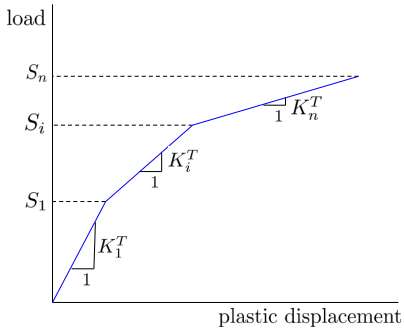

Figure 11: Calibration of the S_i and K_i^T internal parameters from the load-plastic displacement curve.

Elastic stiffness matrix. The elastic stiffness matrix is defined by five coefficients: three of the coefficients describe the elastic lateral response (horizontal, rotational and the coupling between them), one of the coefficients describes the vertical elastic response, and the last coefficient describes the torsional elastic response. For homogeneous soil profiles, these coefficients can be obtained from semi-empirical formulae, see for instance Randolph [39], Gazetas [40] or Doherty et al. [41]. For layered soil profiles, or for changes in soil stiffness with depth not considered in these semi-empirical formulae, the coefficients can be obtained from FEA or from boundary element analyses.

Non-linear load-displacement curves. They can be obtained from static pushover FEA with a soil model that represents the relevant cyclic nonlinear response. Alternatively, model test data can be employed. Two analyses or tests are required to establish these curves: (1) a pushover analyses where a moment is applied at the pile head at seabed, from which $M - u_M$ and $M - \theta_M$ curves are obtained, and (2) a pushover analyses where a horizontal load is applied at the pile head at seabed, from which $H - u_H$ and $H - \theta_H$ curves are obtained.

Altogether, five coefficients and four load-displacement curves are provided as input. With this input, the macro-element model is calibrated internally as follows. First, it computes the plastic displacements as the difference between the elasto-plastic and the elastic components. Then, it determines the coefficients s and β from the relations between the loads and the plastic displacements. After, it builds the transformation matrix $\boldsymbol{R}$ following Eq. 19. The load-plastic displacement relations are transferred to the transformed axis system, where the yield surfaces are 4-dimensional spheres and the same load-plastic displacement curve (illustrated in Fig. 11) is obtained in any radial direction. From the transformed load-plastic displacement relations, the radius S_i, and the plastic stiffness matrix $\boldsymbol{K}_i^p = K_i^p \cdot \boldsymbol{I}$ associated to each yield surface are calculated. Fig. 11 illustrates the derivation of S_i and K_i^T from the load-plastic displacement curve. Then, K_i^p is computed following the assumption that the yield surfaces are coupled

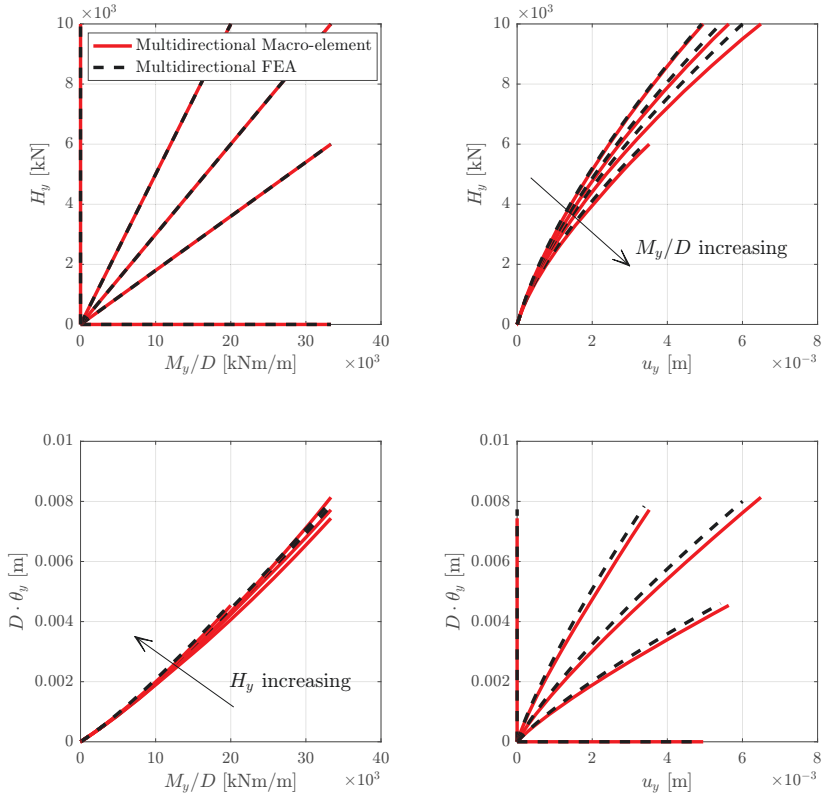

Figure 12: Radial load paths in the $M_y/D - H_y$ and in the $D \cdot \theta_y - u_y$ planes.

in series:

$$K_i^p = \frac{1}{\frac{1}{K_i^T} - \sum_{j=1}^{i-1} \frac{1}{K_j^p}} \tag{22}$$

4.4. Verification against cyclic FEA

The performance of the multidirectional macro-element is ilustrated and compared against FEA for the load combinations presented in Table 4. The pile geometry and soil conditions correspond to those described in Section 3.4.

Fig. 12 show the comparison of the macro-element to monotonic radial paths for a combination of in-plane and out-of-plane loads ($M_y/D - H_y$). The macro-element captures well the load-displacement response and therefore the reduction in stiffness as a consequence of the coupling between in-plane and out-of-plane loads.

Fig. 13 shows the comparison of the macro-element to the rectangular load path also shown in Fig. 7. The objetive of the comparison is to illustrate that the macro-element model can reproduce the multidirectional response described in Section 3.5. The agreement between the macro-element and the FEA is very good, both with regards to the displacement path and the load-displacement curves. This indicates that the yield surface, the flow rule and the hardening law are adequate. Note that every time

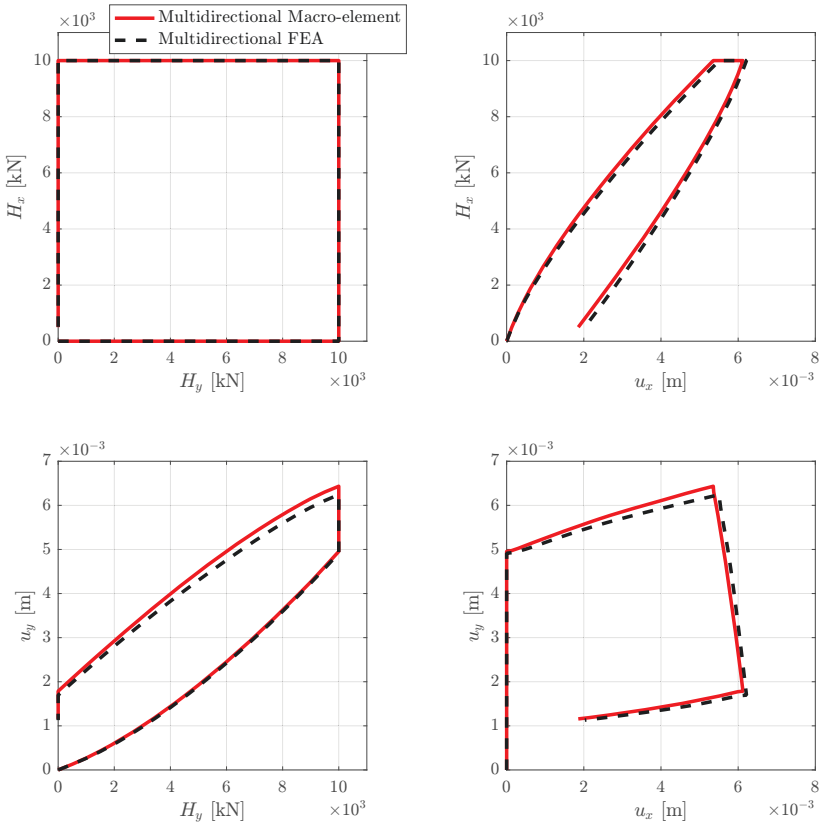

Figure 13: Load and displacement paths in the $H_x - H_y$ and in the $u_x - u_y$ planes for a rectangular load path.

there is a change in the load direction, the initial displacement path is parallel to the load path. This initial displacement path corresponds to the uncoupled elastic response.

Fig. 14 shows the comparison of the macro-element to the bow tie load path. The objective of this comparison is to illustrate that a good fit is also obtained when two out-of-plane loads are increased simultaneously. This is done in a similar manner as the true triaxial test from Nakai [29] introduced in Section 2.2.5.

Finally, two simulated ULS load histories from an OWT are applied to the macro-element and in the FEA. Note that the frequency dependency of the soil and pile response has not been included in the FEA neither in the macro-element model. This is because, for typical soil conditions found in offshore wind farms, it can be neglected at low frequencies, typically below 1-1.5 Hz [42]. The applied loading frequency of the simulated ULS load histories (Figs. 15 and 17) is below this threshold, and therefore no noticeable frequency dependence of the soil response is expected. Figs. 15 and 16 present the load and displacement responses for 30 s simulations before the peak of the simulated ULS storm is reached. Fig. 17 show the comparison for 10 s for the largest part of the simulated ULS storm. The agreement between the macro-element results and the FEA is very good.

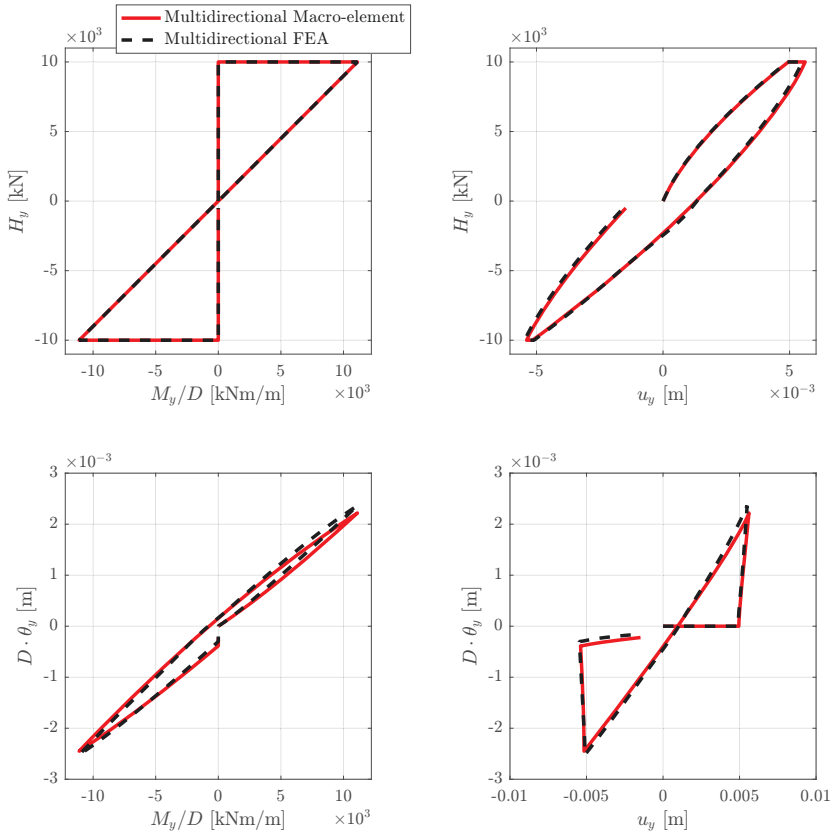

Figure 14: Load and displacement paths in the $H_y - M_y$ and in the $u_y - \theta_y$ planes for a bow tie load path.

5. Discussion

5.1. Impact of multidirectional loading on the monopile response

This section discusses the results from FEA and states the limitations of the numerical study. The main finding of the FEA is that multidirectional loading affects the foundation response at the pile head. The out-of-plane loads affect the in-plane response and viceversa, leading to softer load-displacement curves, as shown in Figs. 7 and 8.

The coupling between in-plane and out-of-plane horizontal loads (see e.g. Fig. 7) is intuitive and it has been observed in small-scale test of slender piles in clay [12, 15]. In particular, Mayoral et al. [15] showed the non-coaxiality between the incremental horizontal forces and the incremental horizontal displacement vectors, which it is also captured in the FEA. However, most of the existing experimental studies in clay focused on describing the $p - y$ response of slender piles, and therefore the coupling between in-plane horizontal loads and out-of-plane moments was not investigated. This coupling has been investigated numerically in this paper, and the results (see e.g. Figs. 8 and 9b) indicate that there is a coupling similar to the coupling between in-plane and out-of-plane horizontal loads. This coupling is observed from relatively small load levels to the load levels corresponding to a ULS storm of an OWT.

It is important to acknowledge the limitations of the numerical study while interpreting the results.

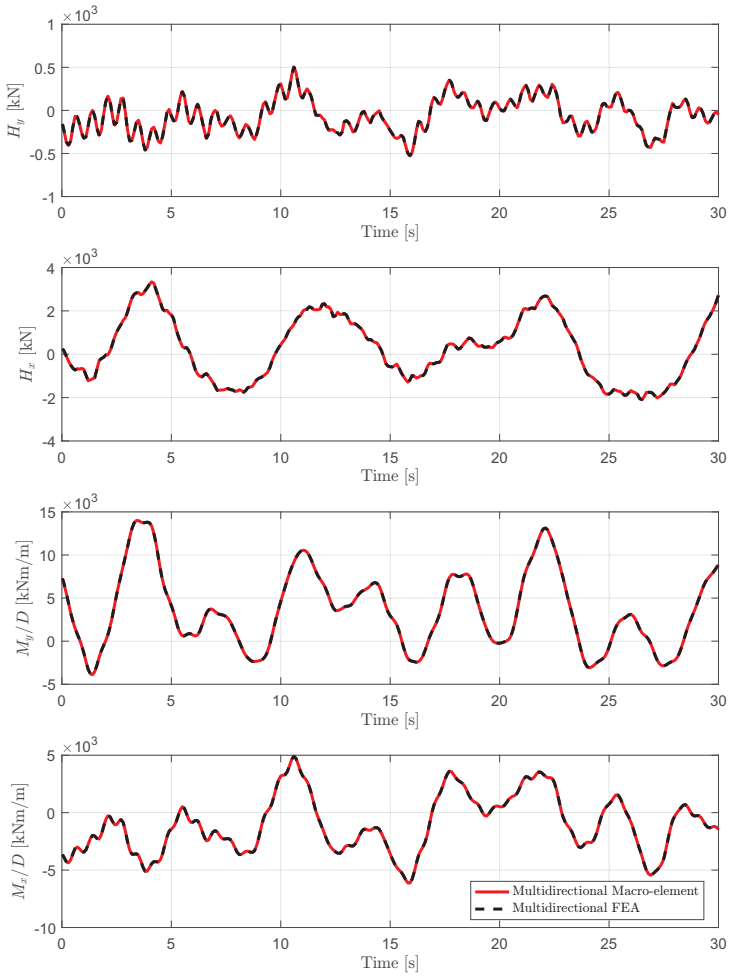

Figure 15: Applied irregular load history from ULS simulations of an OWT.

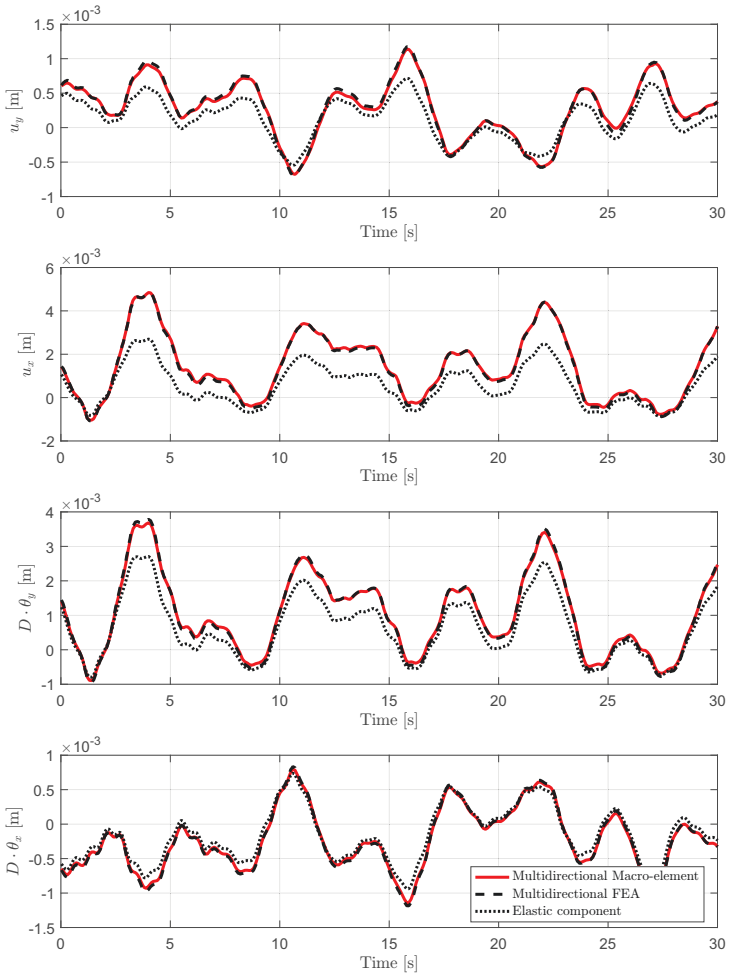

Figure 16: Computed displacements from an irregular load history from ULS simulations of an OWT.

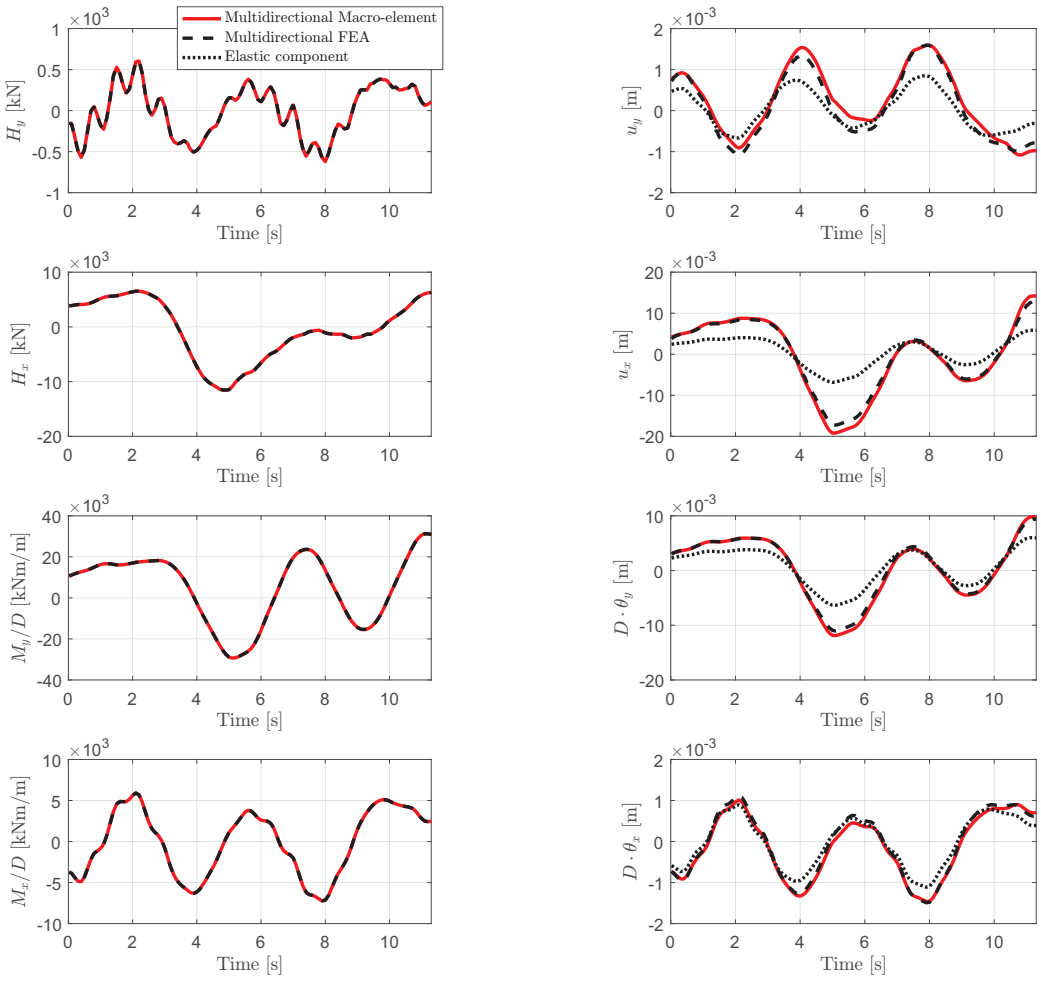

(a) Applied loads vs. time.

(b) Computed displacement vs. time.

Figure 17: Applied loads and computed displacements from the largest loads from ULS simulations of an OWT.

A single pile geometry and soil profile were studied, and the loads were limited to a few seconds of a simulated load history from a 10 MW OWT. The study focused on the behaviour of undrained clay up to the load levels from a ULS storm acting on an OWT, which lead to relatively low mobilisation in the soil. It is also important to note that the results from numerical analyses are highly dependent on the choice of constitutive model. The chosen constitutive model is very simple, and does not account for some features of soil behaviour, e.g. accumulation of strains under cyclic loading. However, the comparison against true triaxial tests indicates that it captures the relevant features during multiaxial 3D stress conditions, while its simplicity guarantees a robust implementation.

Despite these limitations, the numerical study shows that multidirectionality affects the predicted load-displacement response of the foundation, and raises questions with respect to the adequacy of planar models to reproduce multidirectional responses.

5.2. Extension of a foundation model for multidirectional loadings

This section discusses the extension of the formulation of the planar macro-element model described in Page et al. [9] and its verification. The theoretical extension focuses on formulating the yield criterion as a combination of in-plane and out-of-plane loads. It is based on symmetry conditions, in a similar fashion as proposed by Martin [35] and Bienen et al. [34] for shallow foundations.

The agreement between the FEA and the macro-element prediction is very good from low load levels to large load levels corresponding to a ULS storm. This indicates the selected yield criterion, also employed in the flow rule and in the hardening law, is adequate. The yield criterion is formulated as a quadratic form defined by the contours of constant plastic work. This formulation differs from other multidirectional loading macro-element models, see for instance Bienen et al. [34], which define the yield criterion from swipe tests where the vertical displacement is constrained, and therefore the yield surfaces are defined as contours of constant vertical displacement. The main consequence of choosing contours of constant vertical displacement as yield surfaces is that a non-associative flow rule has to be employed, which makes the model implementation more challenging. On this regard, defining the yield surfaces as contours of constant plastic work allows for a simpler and more robust model implementation.

However, the good agreement between the FEA and the macro-element multidirectional prediction has to be taken with care, since it might be a consequence of the constitutive soil model employed in the FEA. This constitutive model follows the same formulation and therefore exhibits the same features (e.g. non-linear hysteretic response) as the macro-element model. Validation with experimental data for the pile dimensions and multidirectional loading conditions representative from OWT would be desirable. However, to the author's knowledge, only experimental results involving planar loads can be found in the literature. A comparison between large-scale field tests and the planar version of the macro-element model is described in Page et al. [9] for pile dimensions representative of OWTs. Good agreement is

found between computed and experimental results.

6. Conclusions

In this paper, a series of FEA have been conducted to assess the effect of multidirectional loading on the response of a monopile in clay. The soil behaviour is simulated with a total stress-based constitutive model capable of reproducing cyclic loading under undrained conditions in time-domain simulations. The results from FEA indicate that the load-displacement response of the pile at seabed is affected by multidirectional loading. This has an impact both on the foundation stiffness and the foundation hysteretic damping, which can modify the natural frequency and damping of the OWT. However, it is often not included in foundation models employed in integrated analyses of OWTs.

A foundation model that accounts for the effect of multidirectional loading is proposed. It follows the macro-element approach, where the response of the pile and the surrounding soil is reduced to a force-displacement relation at seabed. The macro-element model has been developed to represent the foundation response in integrated analyses of OWTs, and it is suitable for this purpose because:

- It can model the non-linear hysteretic load-displacement response observed in pile tests, generating hysteretic foundation damping.
- It accounts for the effect of multidirectional loading.
- The calibration is simple, flexible and it has a physical interpretation.
- It reproduces the response computed by FEA with satisfactory accuracy.
- It is computational efficient. The macro-element model operates as fast as distributed $p-y$ curves in integrated analyses of OWT [10].

Finally, the results provided in this paper are largely based on numerical simulations. Comparison with multidirectional field tests and full-scale measurements of OWT should be carried out to ensure that the numerical results and the formulation of the macro-element model are fair.

7. Acknowledgements

The financial support by the Norwegian Research Council through the project *Reducing cost of offshore wind by integrated structural and geotechnical design (REDWIN)*, Grant No. 243984, is gratefully acknowledged. In addition, we would like to thank Katharina Fechtner for providing useful Python scripts for PLAXIS, and Kristoffer Skjolden Skau for his valuable comments during the development of the research.

References

[1] F. Vorpahl, H. Schwarze, T. Fischer, M. Seidel, J. Jonkman, Offshore wind turbine environment, loads, simulation, and design, Wiley Interdisciplinary Reviews: Energy and Environment 2 (2013) 548–570.

[2] S. Schafhirt, A. Page, G. R. Eiksund, M. Muskulus, Influence of soil parameters on the fatigue lifetime of offshore wind turbines with monopile support structure, Energy Procedia 94 (2016) 347–356.

[3] S. Aasen, A. M. Page, K. S. Skau, T. A. Nygaard, Effect of foundation modelling on the fatigue lifetime of a monopile-based offshore wind turbine, Wind Energy Science 2 (2017) 361.

[4] B. Byrne, G. Houlsby, Foundations for offshore wind turbines, Philosophical Transactions of the Royal Society of London A: Mathematical, Physical and Engineering Sciences 361 (2003) 2909–2930.

[5] D. Kallehave, C. L. Thilsted, M. Liingaard, et al., Modification of the api py formulation of initial stiffness of sand, in: Offshore Site Investigation and Geotechnics: Integrated Technologies-Present and Future, Society of Underwater Technology, 2012.

[6] B. Byrne, R. McAdam, H. Burd, G. Houlsby, C. Martin, L. Zdravković, D. Taborda, D. Potts, R. Jardine, M. Sideri, et al., New design methods for large diameter piles under lateral loading for offshore wind applications, in: 3rd International Symposium on Frontiers in Offshore Geotechnics (ISFOG 2015), Oslo, Norway, June, 2015, pp. 10–12.

[7] M. Damgaard, V. Zania, L. V. Andersen, L. B. Ibsen, Effects of soilstructure interaction on real time dynamic response of offshore wind turbines on monopiles, Engineering Structures 75 (2014) 388–401.

[8] W. Beuckelaers, H. Burd, G. Houlsby, Integrated design method of monopile foundations for offshore wind turbines using a kinematic hardening soil model, in: Proceedings of OSIG 2017 Conference, Society for Underwater Technology, 2017.

[9] A. M. Page, G. Grimstad, G. R. Eiksund, H. P. Jostad, A macro-element pile foundation model for integrated analyses of monopile-based offshore wind turbines, Ocean Engineering 167 (2018) 23 – 35.

[10] A. M. Page, V. Næss, J. B. D. Vaal, G. R. Eiksund, T. A. Nygaard, Impact of Foundation Modelling in Offshore Wind Turbines: Comparison between Simulations and Field Data, Under review in Marine Structures (2018).

[11] N. H. Levy, I. Einav, M. F. Randolph, Effect of recent load history on laterally loaded piles in normally consolidated clay, International Journal of Geomechanics 7 (2007) 277–286.

[12] J. M. Mayoral, J. M. Pestana, R. B. Seed, Determination of multidirectional py curves for soft clays, Geotechnical testing journal 28 (2005) 253–263.

[13] D. Su, Resistance of short, stiff piles to multidirectional lateral loadings, Geotechnical Testing Journal 35 (2011) 313–329.

[14] C. Rudolph, B. Bienen, J. Grabe, Effect of variation of the loading direction on the displacement accumulation of large-diameter piles under cyclic lateral loading in sand, Canadian Geotechnical Journal 51 (2014) 1196–1206.

[15] J. M. Mayoral, J. M. Pestana, R. B. Seed, Multi-directional cyclic p–y curves for soft clays, Ocean Engineering 115 (2016) 1–18.

[16] B. B. Sheil, B. A. McCabe, Biaxial loading of offshore monopiles: numerical modeling, International Journal of Geomechanics 17 (2016) 04016050.

[17] Y. Dafalias, E. Popov, A model of nonlinearly hardening materials for complex loadingein modell für werkstoffe mit nichtlinearer verfestigung unter zusammengesetzter belastung, Acta mechanica 21 (1975) 173–192.

[18] R. Krieg, A practical two surface plasticity theory, Journal of applied mechanics 42 (1975) 641–646.

[19] Z. Mrôz, On the description of anisotropic workhardening, Journal of the Mechanics and Physics of Solids 15 (1967) 163–175.

[20] W. D. Iwan, On a class of models for the yielding behavior of continuous and composite systems, Journal of Applied Mechanics 34 (1967) 612–617.

[21] F.-J. Montáns, Bounding surface plasticity model with extended masing behavior, Computer Methods in Applied Mechanics and Engineering 182 (2000) 135 – 162.

[22] F. J. Montáns, M. A. Caminero, On the consistency of nested surfaces models and their kinematic hardening rules, International journal of solids and structures 44 (2007) 5027–5042.

[23] F. J. Montáns, Implicit multilayer j2-plasticity using prager's translation rule, International Journal for Numerical Methods in Engineering 50 (2001) 347–375.

[24] G. Grimstad, J. Rønningen, H. Nøst, Use of iwan models for modelling anisotropic and cyclic behavior of clays, in: Numerical Methods in Geotechnical Engineering, 2014, pp. 49–54.

[25] R. v. Mises, Mechanik der festen körper im plastisch-deformablen zustand, Nachrichten von der Gesellschaft der Wissenschaften zu Göttingen, Mathematisch-Physikalische Klasse (1913) 582–592.

[26] W. T. Koiter, Stress-strain relations, uniqueness and variational theorems for elastic-plastic materials with a singular yield surface, Quarterly of applied mathematics 11 (1953) 350–354.

[27] A. M. Puzrin, G. T. Houlsby, On the non-intersection dilemma in multiple surface plasticity, Géotechnique 51 (2001) 369–372.

[28] R. Brinkgreve, S. Kumarswamy, W. Swolfs, PLAXIS 2015. Reference Manual, Plaxis bv, 2015.

[29] T. Nakai, Constitutive modeling of geomaterials: principles and applications, CRC Press, 2012.

[30] R. Butterfield, G. T. Houlsby, G. Gottardi, Standardized sign conventions and notation for generally loaded foundations, Géotechnique 47 (1997) 1051–4.

[31] S. R. Vatne, Base case definintion for WAS-XL, Technical Report, SINTEF Ocean AS, 2017.

[32] J. Velarde, E. E. Bachynski, Design and fatigue analysis of monopile foundations to support the dtu 10 mw offshore wind turbine, Energy Procedia 137 (2017) 3–13.

[33] K. Andersen, Cyclic soil parameters for offshore foundation design, Frontiers in offshore geotechnics III (2015) 5–82.

[34] B. Bienen, B. Byrne, G. Houlsby, M. Cassidy, Investigating six-degree-of-freedom loading of shallow foundations on sand, Géotechnique 56 (2006) 367–379.

[35] C. Martin, Physical and numerical modelling of offshore foundations under combined loads (1994).

[36] K. S. Skau, G. Grimstad, A. M. Page, G. R. Eiksund, H. P. Jostad, A macro-element for integrated time domain analyses representing bucket foundations for offshore wind turbines, Under review in Marine Structures (2017).

[37] T. A. Nygaard, J. De Vaal, F. Pierella, L. Oggiano, R. Stenbro, Development, verification and validation of 3Dfloat; aero-servo-hydro-elastic computations of offshore structures, Energy Procedia 94 (2016) 425–433.

[38] MARINTEK, SIMA 3.2 User Guide, Technical Report, MARINTEK, 2015.

[39] M. F. Randolph, The response of flexible piles to lateral loading, Géotechnique 31 (1981) 247–259.

[40] G. Gazetas, Foundation vibrations, in: Foundation engineering handbook, Springer, 1991, pp. 553–593.

[41] J. Doherty, G. Houlsby, A. Deeks, Stiffness of flexible caisson foundations embedded in nonhomogeneous elastic soil, Journal of geotechnical and geoenvironmental engineering 131 (2005) 1498–1508.

[42] M. Shadlou, S. Bhattacharya, Dynamic stiffness of pile in a layered elastic continuum, Geotechnique 64 (2014) 303.